Research paper

X-ray studies on the nano- and microscale anisotropy in compacted clays: Comparison of bentonite and purified calcium montmorillonite

Jussi-Petteri Suuronen [a],[*],[1], Michał Matusewicz [b], Markus Olin [b], Ritva Serimaa [a]

[a] Department of Physics, University of Helsinki, P.O.B. 64, FI-00014 University of Helsinki, Finland
[b] VTT Technical Research Centre of Finland, Otakaari 3K, Espoo, P.O. Box 1000, FI-02044 VTT, Finland

A B S T R A C T

Exceptional water retention properties make compacted clays and clayrocks attractive materials in waste management applications, e.g. as buffer materials and barrier formations for radionuclide release in geological disposal of spent nuclear fuel elements. Consisting of particles with a very high aspect ratio, clay materials exhibit significant structural anisotropy with potential implications on their performance. In this work, the micron-scale and nanometer-scale anisotropy in compacted calcium montmorillonite and MX-80 bentonite were investigated and quantified under varying humidity conditions; the utilized novel experimental method combines X-ray microtomography (XMT) and small-angle X-ray diffraction to near-simultaneously characterize both the micron-scale 3D morphology and mineralogical properties such as clay platelet spacing in platelet stacks (tactoids) and tactoid orientation. Sedimentation during the purification process and lack of accessory minerals were found to induce much stronger orientation in purified Ca-montmorillonite as compared to the MX-80. In highly anisotropic samples, the orientation of microcracks visualized with XMT under low humidity conditions was found to correlate with the local orientation of clay tactoids measured with X-ray diffraction. The proposed experimental method can be applied to a wide range of similar materials, such as shales or samples from clayrock formations.

© 2014 Elsevier B.V. All rights reserved.

1. Introduction

In the final disposal of spent nuclear fuel the basic principles are isolation and encapsulation. The latter is typically based on two barriers: a metal based canister surrounded by a buffer, which is aimed to prevent corrosion and dampen any dislocations of the surrounding bedrock or clay. The buffer material must therefore have very low water conductivity in order to limit mass transport to diffusion, but the buffer must also be ductile enough for dampening purposes. Most commonly applied buffer materials include smectite group swelling minerals; bentonite is a clay material having a high amount of sodium montmorillonite and some other minerals.

The use of swelling clays such as bentonite as buffer materials or liners in waste disposal applications relies largely on the capacity of the montmorillonite to absorb water in the interlayer space in stacks formed of several clay layers, which causes the stack (i.e. tactoid) to swell in the direction perpendicular to the layers (e.g. Norrish, 1954; Salles et al., 2008). A direct consequence of this behavior is that in a well-oriented mass of clay material, like that produced by uniaxial compaction, also the mechanical and transport properties of the mass could be anisotropic. In addition to interlayer water, bentonite is widely considered to contain some porewater in the spaces between individual clay tactoids (e.g. Bradbury and Bayens, 2003; Muurinen and Carlsson, 2013), although the relative volumes of the two porosity types are still under debate.

In the KBS method for a spent nuclear fuel repository chosen to be applied in Finland and Sweden (SKB, 2011; Posiva, 2012), a compacted bentonite buffer is designed not only to absorb water leaking into the tunnel and seal off any cracks present at installation, but also to limit the release of radionuclides into the environment through their slow diffusive transport within the buffer. Additionally, the buffer provides mechanical shielding to the copper/cast iron canister containing the used fuel elements. The effect of preferred tactoid orientation (sometimes also called the 'texture' or 'fabric' in the literature) on the diffusion speed is therefore especially of interest, and experiments have been made to quantify this diffusion anisotropy (Sato and Suzuki, 2003; Suzuki et al., 2004). The results of Sato and Suzuki suggest that the diffusion anisotropy becomes more significant with increasing clay mineral content of the mass.

The effect of preferred orientation on clay properties is even more pronounced in waste disposal concepts that depend on clayrock or shale formations as natural release barriers surrounding the repository, such as those under consideration in Switzerland (Nagra, 2002) and

* Corresponding author. Tel.: +358 503559524.
E-mail addresses: jussi-petteri.suuronen@helsinki.fi, jussi-petteri.suuronen@esrf.fr
(J.-P. Suuronen), michal.matusewicz@vtt.fi (M. Matusewicz), markus.olin@vtt.fi (M. Olin),
ritva.serimaa@helsinki.fi (R. Serimaa).
[1] Present address: European Synchrotron Radiation Facility, Experiments division,
38043 Grenoble, France. Tel.: +33 4 76882909.

France (Andra, 2011). Preferred orientation in these systems has received considerable attention, through e.g. X-ray diffraction experiments of clay particle orientation (Wenk et al., 2008) or high-resolution 3D electron microscopy of the pore space geometry (Keller et al., 2011). Kanitpanyacharoen et al. (2011, 2012) have also combined synchrotron X-ray microtomography with diffraction analyses and electron microscopy to incorporate information about micrometer-scale features in shales into the analysis. In Opalinus Clay, anisotropy has also been recently observed in the field-scale diffusive transport of radiotracers (Gimmi et al., 2014).

X-ray microtomography (XMT, also known in the literature as μCT) has also been applied to materials intended for engineered barriers, such as compacted bentonite–quartz mixtures and bentonite ore (Kawaragi et al., 2009; Saba et al., 2014a, 2014b), and compared with hydraulic conductivity measurements and mercury intrusion porosimetry. A conclusion of Kawaragi and coworkers was that the water permeability of bentonite ore is independent of the sedimentary texture. Unfortunately, however, anisotropy in the water permeability of the compacted material is not discussed, and the results on bentonite ore may not be directly applicable to the processed and compacted material. While modern synchrotron radiation facilities are available for resolution in the nanometer range, a typical XMT setup loses somewhat in resolution compared with other three-dimensional imaging methods such as focused ion beam (FIB) tomography (Holzer et al., 2010). With an imaging system able to visualize porosities and impurities only in the micrometer length scale, complementary methods are needed to evaluate characteristics on the level of individual clay particles. On the other hand, XMT is non-destructive and often requires only minimal sample preparation, making it ideal for studies of time-dependent processes (4D imaging), and avoiding potential artifacts due to e.g. cutting or freezing of samples often required in electron microscopy applications. An overview of the technique and its potential uses in geosciences is given by Cnudde and Boone (2013).

In this work, we aim to complement the previous studies on the behavior of various bentonite or montmorillonite-containing materials with a detailed analysis of the structural anisotropy in samples of pure MX-80 bentonite or purified Ca-montmorillonite at varying levels of water saturation. The experiments were performed with a novel experimental setup (Suuronen et al., 2014), that allows both XMT imaging of any microcracks and impurities within the material, and determination of the local mineralogy (tactoid orientation and interlayer spacing) using microbeam small-angle X-ray diffraction (SAXD). An advantage over previous X-ray or neutron diffraction studies (e.g. Bihannic et al., 2001; Devineau et al., 2006; Holmboe et al., 2012; Matusewicz et al., 2013) is that the path of the diffracting X-ray beam within the volume imaged by XMT is known to within approximately 200 μm.

2. Materials and methods

2.1. Sample preparation

The clay used in the experiments was Wyoming MX-80 bentonite (CETCO, UK). Ca-montmorillonite was obtained by purification of MX-80 using the method of Tributh and Lagaly (1986). It consisted of separation of coarse particles by centrifugation followed by removal of remaining carbonates, iron oxides and organic material by treatment with acetate buffer, citrate buffer and hydrogen peroxide respectively. Purified clay was washed with 1 M $CaCl_2$ three times to obtain homoionic Ca-montmorillonite. Excess of salt was removed by dialysis after which the montmorillonite was freeze-dried and ground to grain size <1 mm. This size was chosen to match the MX-80 grain size (Juvankoski, 2013). Clay in an air-dry state was compacted uniaxially into four pellets (two pellets each of MX-80 and purified Ca-montmorillonite, diameter 20 mm, height 10 mm) and closed in cells where it was water saturated and left to equilibrate for a minimum of three months. Both MilliQ water and 0.1 M perchlorate solution (Na-perchlorate for MX-80, Ca-perchlorate for the purified samples)

were used for equilibration. Contact with the equilibrating solution was ensured through sinters of 2 μm pore size.

After opening the equilibration cells, the pellets were sampled by forcing a small diameter (0.8 mm, wall thickness 200 μm) polyether-ether-ketone (PEEK) capillary through the compacted pellet in the direction of compaction. To rule out sampling artifacts from the observations, control samples were also taken in the direction perpendicular to the axis of compaction of the Ca-montmorillonite equilibrated in the perchlorate solution. For humidity control during the microtomography and small angle diffraction experiments, an approximately 5 mm section of the capillary was mounted on the sample holder shown in Fig. 1: the sample is mounted upright on a steel rod, which is surrounded by a cup filled with liquid and covered with a plastic cap with a small drop of liquid at the top. The plastic cap and capillary are fairly transparent to x-rays, enabling the tomography and diffraction experiments while maintaining a fixed relative humidity (RH) within the holder. For the initial measurements of each sample, the liquid inside the holder was taken from the equilibration cell, keeping the samples as close as possible to the saturation conditions. To reduce the humidity, the liquid was exchanged with a saturated potassium chloride (KCl) solution, giving approximately 85% RH at the temperature of the measurement room, which is maintained at 25 °C or lower (Greenspan, 1976). For the final experiments on each sample, the humidity was reduced to ambient RH (20–32%) by removing the liquid and the plastic cover. The sample was allowed to settle for a minimum of 12 h at each humidity step. This was deemed sufficient by comparing radiographs taken at the beginning and end of the microtomography scan (approximately 2 h); if necessary, the scan was repeated after further settling time. The dry density of the saturated samples was checked by weighing a small piece of the pellet immediately after opening the equilibration cell, and after drying at 105 °C for several hours, until no change in the mass was observed in subsequent weightings. The dry density was found to be 1.5 g/cm^3 for both Ca-montmorillonite samples and 1.6 g/cm^3 for the MX-80 samples.

2.2. X-ray microtomography and diffraction measurements

The combined microtomography and diffraction system is based on a high-resolution XMT scanner Nanotom 180 NF (Phoenix X-ray Systems and Services Gmbh, presently part of GE Measurement and Control Solutions, Germany) that has been constructed inside a large lead-shielded room to accommodate an additional microfocus X-ray tube (IμS, Incoatec GmbH, Germany) and detector (Pilatus 1 M, Dectris Ltd., Switzerland) that allow small-angle X-ray scattering or X-ray diffraction studies to be carried out on a specified sub-volume of the
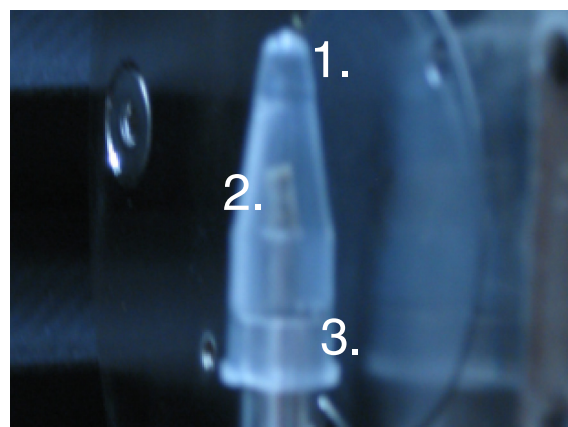

Fig. 1. The sample environment used, positioned as close as possible to the X-ray source. Markings: the liquid droplet at the top of the plastic cover (1.), the sample inside a PEEK capillary (2.), and the metal cup containing the liquid for humidity control (3.).
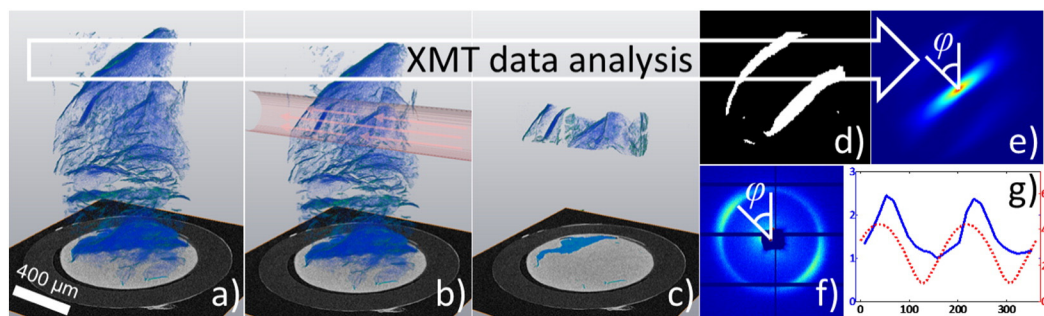
Fig. 2. Analysis of microcrack orientation from XMT data. a) Volume rendering of the XMT data, with low gray values (i.e. pores) within the sample rendered in blue and high gray values transparent. The horizontal slice through the data shows the standard coloring with brightness of the voxel corresponding to gray value. b) The volume is sampled by the diffracting beam approximated by a cylinder of 200 μm diameter. The beam is propagating from right to left in the image. c) Intersection of the pore space with the scattering beam. d) One slice through the binarized porosity dataset in the direction of the diffracting beam. e) Sum of 2D autocorrelations of all slices within the diffracting beam. f) Corresponding SAXD pattern. g) Plot of R (blue line, left scale) and v (red dashed line, right scale) versus the azimuthal angle φ, calculated based on e) and f). (For interpretation of the references to color in this figure legend, the reader is referred to the web version of this article.)

sample, based on the XMT reconstruction. The diameter of the diffracting X-ray beam can be adjusted; for these experiments a typical value of 200 μm was used. For details, the reader is referred to Suuronen et al. (2014).

2.3. XMT measurements

The Nanotom 180 NF system consists of a nanofocus end-window x-ray tube, a sample manipulator stage and a 5 megapixel CMOS detector (Hamamatsu Photonics, Japan). For XMT scanning, the sample holder was placed as close as possible to the X-ray source in order to maximize resolution while minimizing the source-to-detector distance to increase the intensity of X-rays hitting the detector. The imaging geometry resulted in an isotropic voxel size (edge length of one cubical volume element) of 1.0–1.2 μm; the scan parameters were varied slightly to compensate for some encountered beam stability issues, as well as to save time in the case of Ca-montmorillonite samples at 100% RH, where image noise was less important. A total of 720 to 1200 transmission radiographs were taken of each sample, as an average of 4–10 × 500 ms exposures over a 360° rotation. The X-ray tube voltage was 60–90 kV and current 150–220 μA. Datos|x software supplied by the equipment manufacturer was used for tomographic reconstruction of the transmission images.

2.4. Small-angle diffraction measurements

After XMT scanning, 2–5 SAXD measurements were carried out on each capillary, directing the X-ray beam at different observation points within the samples. Molybdenum K_α–radiation (wavelength $\lambda = 0.7108$ Å) was focused and monochromated with Montel optics attached to the microfocus X-ray tube[2]. The X-ray tube voltage and current were 50 kV and 600 μA. The diffraction patterns were obtained in the perpendicular transmission geometry as the sum of 3 × 15 min exposures, and processed with a Matlab algorithm to eliminate 'speckles', or isolated pixels with erroneously high intensity that are characteristic of the Pilatus detector. Diffraction from a silver behenate standard was used to calibrate the sample-to-detector distance. The analyzed range of scattering vector magnitude (q-value) was $q = 0.2$–1.0 Å^{-1}, corresponding to an interlayer spacing of $d = 6.3$–31.4 Å, according to the relation $d = 2\pi/q$. The q-value is used instead of the scattering angle 2θ, since it provides a wavelength-independent measure for the observed structural period. The two are related according to the equation $q = \frac{4\pi \sin\theta}{\lambda}$.

2.5. Data analysis

The data analysis workflow for comparing microcrack orientation (visible in the XMT images) with clay tactoid orientation (quantified from SAXD patterns) is shown in Fig. 2. The image processing of the 3D reconstructions was carried out in Avizo Fire Edition software (v. 7.2 and 8.0.1, FEI, USA). After noise-removal filtering with a 3 × 3 × 3 voxel bilateral filter and separation of the sample volume from the PEEK capillary (Fig. 2a), the volume sampled by the diffracting beam was isolated (Fig. 2b–c) and binarized with a dual-threshold algorithm, that divides the voxels into three classes based on manually set gray value limits: dark (pore) voxels, intermediate gray value, and light (clay) voxels. Of the intermediate class, all voxels connected to dark voxels within a set distance were also included in the pore space (Fig. 2d). The porosity was calculated as the ratio of pore voxel volume to the total sample volume irradiated by the scattering beam. The binary volume corresponding to the scattering beam path was then imported to Matlab software (v. r2013a, Mathworks Inc., USA), and processed with a custom-written MATLAB program to calculate the 2D autocorrelation of each slice perpendicular to the diffracting beam. These autocorrelations are then summed (Fig. 2e), and compared with the scattering pattern recorded during the diffraction experiment (Fig. 2f). Also the porosity within each sub-volume was calculated from the binary data.

After background subtraction, the recorded SAXD patterns were analyzed both in terms of intensity versus q-value and intensity of the montmorillonite (001)-peak versus azimuthal angle φ.

In order to quantitatively compare the preferred orientation observed in the autocorrelation of the XMT data with that seen in the diffraction pattern, the following computations were performed for each autocorrelation image–diffraction pattern pair:

- The autocorrelation image is symmetric with respect to a central maximum, so for each angle φi (in 7.5° steps), we find the distance d_i, where the value of the autocorrelation drops to one half of the maximum. This is done through interpolating the data along a line through the center.
- The *autocorrelation descent speed* for each φ_i is defined as $v_i = d_{max}/d_i$, where d_{max} is the longest measured half-distance.
- The relative intensity of the 001-peak with respect to the minimum is defined in a similar fashion (sampling the data in 15° wedges to reduce the effects of gaps between detector modules): $R_i = I_i/I_{min}$, where I_{min} is the smallest intensity.

For a perfectly isotropic sample, plotting either v or R versus φ (as in Fig. 2g) should yield a flat line at unity; the maximum values on these curves, denoted R_{max} and v_{max} in the results, give direct measures of the degree of orientation in the nano- and microscale. It should also be noted that with this definition, it is impossible for either R or v to

---

[2] One ångström (Å) equals 10^{-10} m.

achieve a value less than one and that the number of maxima in the curve yields the type of symmetry in the diffraction pattern: in this case we expect a two-fold symmetry, or 2 distinct maxima with 180° separation.

3. Results

3.1. XMT measurements

Fig. 3 shows vertical cross-sections of the samples in different humidity conditions. At nearly 100% humidity (with the equilibrating solution in the sample holder), there are only a few pores visible within the samples. The Ca-montmorillonite samples in particular look very homogeneous due to poor contrast between water-filled micropores and the clay material. In the MX-80, accessory mineral grains are easily visible and provide a point of reference for assessing the shrinkage of the clay matrix as the sample is dried. In Ca-montmorillonite, a reduction in RH results in increased porosity in the form of microcracks, which can be seen to begin developing at 85% RH, and are numerous at 20–30% humidity. In MX-80, on the other hand, significant porosity is developed already at 85% RH in the perchlorate-equilibrated sample, while the water-equilibrated sample is markedly less porous even at 32% RH. Comparing the orientation of the microcracks at ambient humidity (see also 3D renderings of the pore space in Fig. 4), they can be seen to have a predominantly horizontal orientation in the purified Ca-montmorillonite and appear more randomly oriented in MX-80. In MX-80, some cracks are also seen to follow the sides of accessory mineral grains. Note that in both perchlorate-equilibrated samples, the clay column seems to have broken during the sampling, which results in widening gaps between column parts as the clay shrinks; while included in the data in Table 2, these are not technically porosities as they span the entire width of the capillary, and have not been rendered in Fig. 4. The orientation of microcracks perpendicular to the axis of compaction in Ca-montmorillonite was also confirmed by the control capillaries sampled perpendicularly to the axis of compaction, though the porosity in these was lower since the clay was shrinking along the short dimension of the samples.

3.2. SAXD measurements

Plots of scattered intensity versus q-value for each sample are shown in Fig. 5. Qualitatively, all SAXD curves obtained at different positions of the same sample under fixed humidity show the same features, so all curves have been summed to improve the statistical quality of the data. The interlayer spacings corresponding to the 001-peaks in each sample are given in Table 1, showing the expected trend towards lower values with reduced humidity.

3.3. Comparison between orientation in XMT and SAXD

Qualitatively, the preferred orientation seen in SAXD patterns can be seen to correlate with the local orientation of microcracks in the Ca-montmorillonite at low humidity, especially in the sample equilibrated with MilliQ water (Fig. 6). In MX-80, data with both methods appears significantly more isotropic.

Values for the orientation parameters calculated as explained in Section 2.4, along with porosities calculated from the XMT data, are given in Table 2. In Ca-montmorillonite, similarly aligned microcracks are formed in areas where the SAXD pattern is highly oriented with R_{max} higher than 2.0 (see Fig. 7).

4. Discussion

4.1. Characterization of anisotropy in compacted bentonite

In light of the results, the microstructure of the montmorillonite phase in compacted bentonite seems dependent on the presence of impurities within the clay: purified Ca-montmorillonite samples generally show strong preferred orientation of tactoids, while in MX-80 the montmorillonite remains isotropic despite the compaction. Although the observed orientation axis in Ca-montmorillonite does not always coincide with the compaction axis, it would be reasonable to assume that this will be the case in bulk compacted montmorillonite: the discrepancies are likely due to rheological effects (material sticking to the capillary walls during sampling) and inaccuracies in performing the sampling and sample
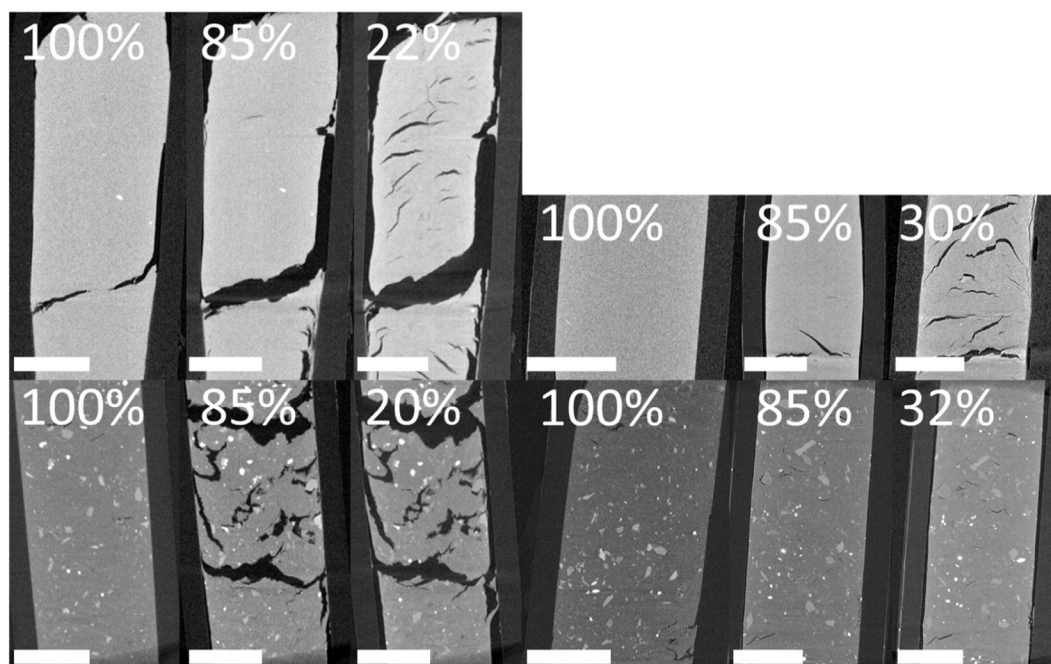

Fig. 3. Vertical XMT sections of Ca-montmorillonite (top row) and MX-80 (bottom row) samples equilibrated in 0.1 M salt solution (left half of the figure) and in milliQ water (right half of the figure). The percentages in each panel indicate RH, white scale bars equal 500 μm.
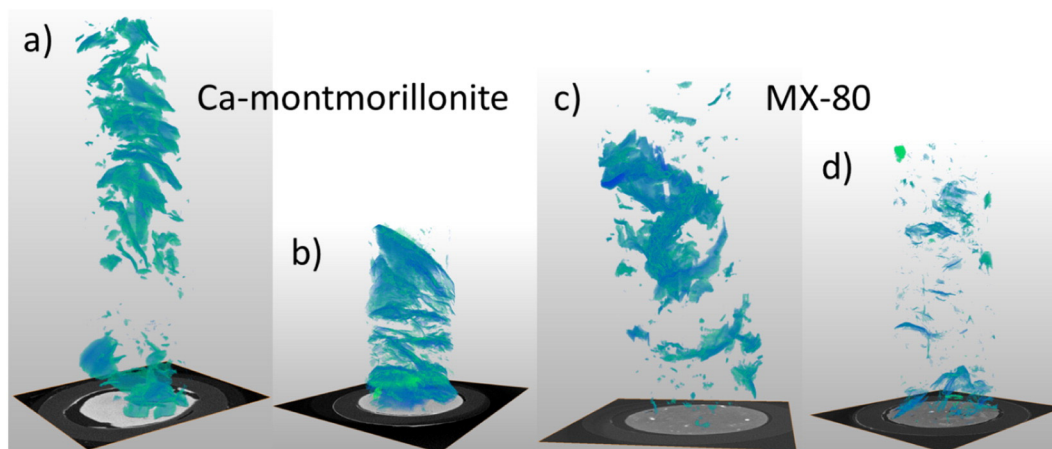
Fig. 4. 3D-renderings of the pore space observed with XMT in the samples at ambient humidity. a) and c) are the samples equilibrated in 0.1 M perchlorate solution and b) and d) those equilibrated in MilliQ water.

mounting exactly vertically. Moreover, whenever strongly preferred orientation of the tactoids was found, also the microcracks that develop in low humidity were found to be aligned in the same direction. This can be taken to indicate that montmorillonite particles preferentially attach face-to-face during compaction, and agglomerates of the particles tend to break up with the void appearing along the face of a particle, rather than at edge-to-edge contacts. This observation is similar to the findings of Sato and Suzuki (2003), who analyzed bentonites of two different montmorillonite contents (approximately 50% and 100%) through SEM imaging and measurement of the apparent diffusion coefficients for deuterated and tritiated water. Their conclusion was that while nearly pure montmorillonite is highly anisotropic after uniaxial compaction, the presence of impurities makes the clay material more isotropic, while also increasing the overall effective diffusion coefficients. The anisotropy in effective diffusion coefficient for deuterated water in bentonites of high montmorillonite content was also observed by Suzuki et al. (2004), with diffusion being significantly faster in the direction perpendicular to the compaction axis than in the parallel direction.

One possible reason for the anisotropy-decreasing effect of impurities can be qualitatively understood by considering the accessory minerals as essentially incompressible at the pressures induced during compaction: their presence then disturbs the stress field during compaction, preventing the tactoids from achieving a closely packed
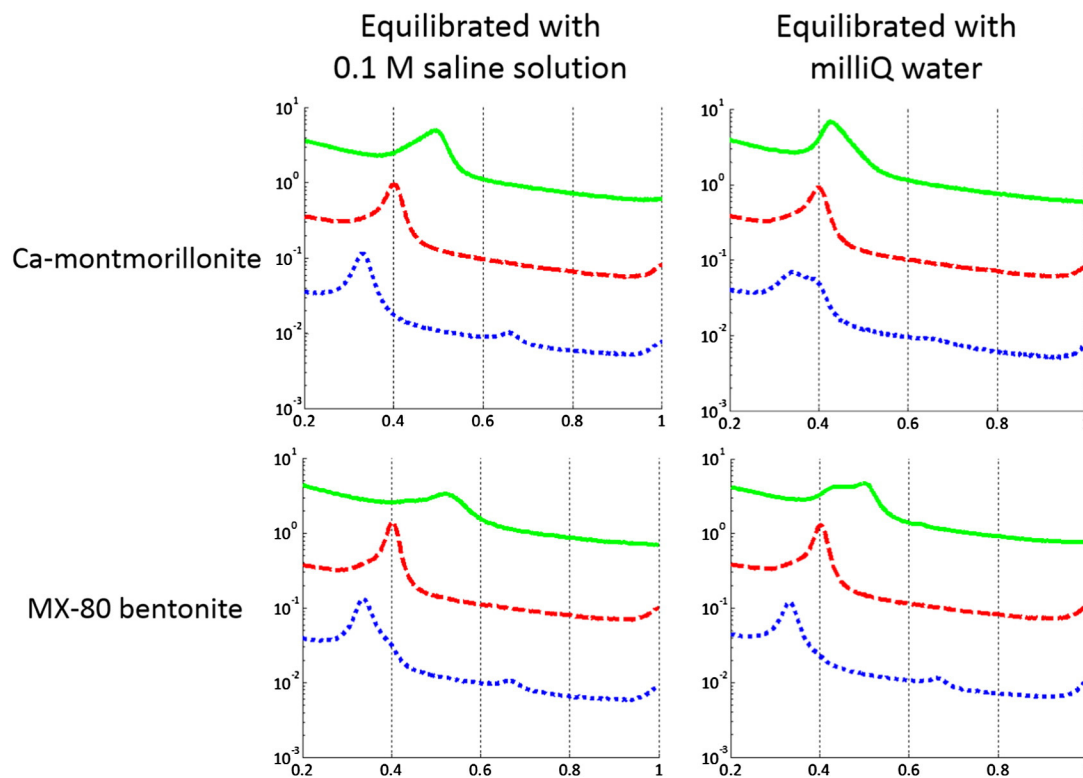

Fig. 5. SAXD patterns of the samples (2–5 measurements per sample summed to improve counting statistics). The horizontal axis is q-value in Å^{-1}, vertical axis intensity in arbitrary units. Note the logarithmic scale, the lines have been offset to improve clarity. Dotted blue lines correspond to the measurements with the equilibrating solution in the sample holder (~100% RH), dashed red lines to saturated KCl solution (~85% RH), and solid green lines to ambient humidity (20–32% RH depending on the sample). (For interpretation of the references to color in this figure legend, the reader is referred to the web version of this article.)

Table 1
Observed interlayer spacings as a function of clay type and RH.

Clay type	Equilibrating solution	RH [%]	Mean d-spacing [Å] (2–5 measurements)[a]
Ca-montmorillonite	0.1 M Ca(ClO$_4$)$_2$	100%	19.0
		85%	15.7
		22%	12.7
	MilliQ water	100%	18.4
		85%	15.8
		30%	14.8
MX-80	0.1 M NaClO$_4$	100%	18.7
		85%	15.6
		20%	12.1
	MilliQ water	100%	18.9
		85%	15.6
		32%	12.5

[a] Value at which the highest intensity is observed in the 001 peak.

structure. The appearance of microcracks along accessory mineral grain boundaries would also indicate a tendency of tactoids to align with the accessory mineral grains, resulting in a conceptual model for the structure very much like that presented by Sato and Suzuki. An interesting open question remains whether these microcracks appear at random locations within the clay mass, or at the locations of water-filled (and thus invisible in XMT) non-interlayer pores or grain boundaries in the saturated material. In the latter case, the cracking pattern in dried clay could be used to retrospectively evaluate the pore network within the saturated sample.

Another factor enhancing the preferred orientation in Ca-montmorillonite samples can be the purification process, in which the clay mineral is dried from a suspension and the clay layers are likely to sediment in an organized way. As the grinding produces a grain size comparable to the capillary diameter, the orientation seen in the experiments can be influenced by the purification process.

Considering the potential use of bentonite in an HLW repository, the MX-80 shows a very isotropic structure in terms of clay tactoid orientation, nor is there any easily observed anisotropy in the morphology or distribution of the accessory minerals. However, the desired swelling and retention properties of bentonite are due to the montmorillonite content, which creates an incentive to use a relatively pure montmorillonite as the buffer material. The results shown here indicate that with pure compacted montmorillonite, the induced anisotropy is a potential design consideration, and definitely should be a factor when transport or mechanical models of the buffer are based on data obtained with purified montmorillonite.

4.2. Qualitative properties of the SAXD curves

In terms of interlayer spacing, all samples showed similar behavior, with the dominant spacing shifting from approximately slightly below or exactly 19 Å in the saturated samples, to approximately 15.7 Å at 85% RH and around 12.5 Å at lower humidities. The sole outlier is the Ca-montmorillonite equilibrated with MilliQ water, which showed a maximum scattered intensity corresponding to 14.8 Å at 30% RH. It should be noted, however, that also for the other samples, the SAXD curve at ambient humidity shows a shoulder towards the low-q side of the 001 peak, and with MilliQ water-equilibrated MX-80 the peak could even be considered bimodal. This is also the case for the SAXD measurements at 85% RH, but in the saturated samples, the tail of the peak is found towards high q-values. In terms of water molecule layers between the clay layers, the observed d-spacings correspond approximately to three layers (18.4–19 Å) at saturation, two layers (15.2–15.7 Å) at RH 85%, and one layer (12.2–12.7 Å) at ambient humidity (Holmboe et al., 2012). However, as witnessed by the above mentioned peak at an intermediate q-value between one and two water layers and the long tails and bifurcation of peaks observed in other samples, montmorillonite stacks in two hydration states are present simultaneously. These materials thus also exhibit shrinkage heterogeneity in addition to swelling heterogeneity already observed by other authors (Ferrage et al., 2005; Devineau et al., 2006). The disappearance of the second-order diffraction peak (002) at lower humidities can be attributed to interstratification, or the coexistence of different hydration states within the same stack, as previously observed for high dry density Ca-montmorillonite (Matusewicz et al., 2013). It should be noted that even though there was significant heterogeneity within the samples in terms of tactoid orientation and microscale porosity, the radially averaged SAXD curves only showed minor differences at different measurement points in the same sample. The humidity conditions can then be considered to be homogeneous, and the stabilization time in the set humidity to be adequate.

4.3. Further applications of the methodology

The experimental and analysis methodology presented in this paper is by no means restricted to bentonite samples (see e.g. Suuronen et al., 2014; Kohout et al., 2014 for an example on mineralogical and XMT analysis of micrometeorites): the limiting factor is that the molybdenum K$_\alpha$-radiation used for the diffracting beam must be able to penetrate the sample, at least in the position and direction chosen for
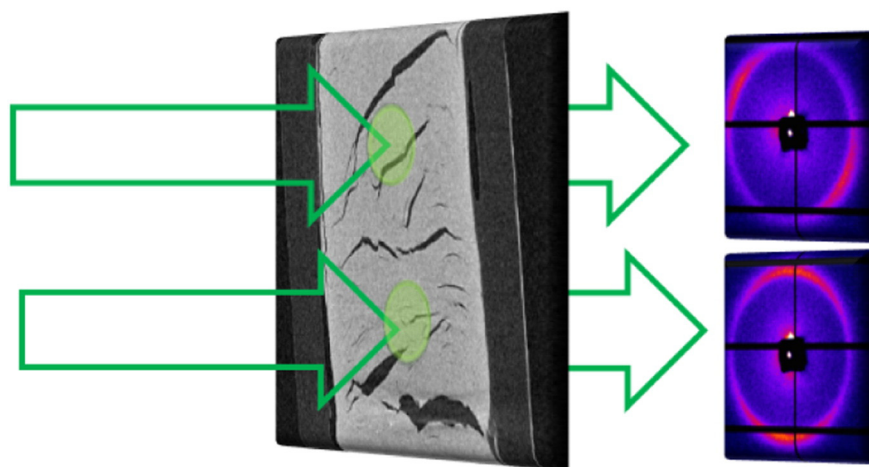

Fig. 6. Qualitative observation of correlation between the orientation of microcracks visible in the vertical XMT section and preferred orientation of tactoids seen in the SAXD patterns (right). Green arrows and overlay circles in the XMT slice indicate the area sampled by the SAXD measurements. (For interpretation of the references to color in this figure legend, the reader is referred to the web version of this article.)

Table 2
Orientation parameters and porosity calculated for each SAXD measurement and XMT data of the sampled volume. N/A signifies that porosity of the XMT data was too low for detection. $\varphi = 0°$ corresponds approximately to the axis of compaction.

Ca-montmorillonite, Ca(ClO$_4$)$_2$ equilibrated

RH [%]	R_{max}	v_{max}	$\varphi_{maximum}$ (SAXD) [°]	$\varphi_{maximum}$ (XMT) [°]	Difference [°]	Porosity based on XMT
100	2.3	N/A	127.5	N/A	N/A	N/A
	1.7	N/A	247.5	N/A	N/A	N/A
	1.8	3.6	352.5	337.5	15.0	0.025
	1.7	3.0	82.5	172.5	90.0	0.079
85	2.2	N/A	127.5	N/A	N/A	N/A
	3.8	N/A	82.5	N/A	N/A	N/A
	2.1	2.1	352.5	187.5	15.0	0.039[a]
	1.9	1.3	82.5	202.5	60.0	0.011
22	3.4	2.1	157.5	157.5	0.0	0.048
	1.9	2.3	172.5	172.5	0.0	0.068
	1.8	1.4	112.5	127.5	15.0	0.006
	3.8	2.3	262.5	45.0	37.5	0.042

MX-80, NaClO$_4$ equilibrated

RH [%]	R_{max}	v_{max}	$\varphi_{maximum}$ (SAXD) [°]	$\varphi_{maximum}$ (XMT) [°]	Difference [°]	Porosity based on XMT
100	1.1	3.8	67.5	202.5	45.0	0.013
	1.2	2.5	67.5	195.0	52.5	0.020
	1.2	N/A	97.5	N/A	N/A	N/A
	1.2	N/A	97.5	N/A	N/A	N/A
85	1.1	1.3	172.5	142.5	30.0	0.098
	1.2	1.7	82.5	135.0	52.5	0.044
	1.1	1.9	82.5	157.5	75.0	0.302[a]
	1.2	1.7	82.5	0.0	82.5	0.171[a]
22	1.1	1.5	112.5	285.0	7.5	0.109
	1.1	1.6	52.5	135.0	82.5	0.042
	1.1	2.2	82.5	157.5	75.0	0.074[a]
	1.2	2.2	97.5	172.5	75.0	0.115[a]

Ca-montmorillonite, MilliQ water equilibrated

RH [%]	R_{max}	v_{max}	$\varphi_{maximum}$ (SAXD) [°]	$\varphi_{maximum}$ (XMT) [°]	Difference [°]	Porosity based on XMT
100	2.2	N/A	127.5	N/A	N/A	N/A
	2.3	N/A	142.5	N/A	N/A	N/A
85	2.4	N/A	307.5	N/A	N/A	N/A
	2.5	N/A	127.5	N/A	N/A	N/A
	4.1	2.6	337.5	330.0	7.5	0.047
	2.7	2.4	22.5	7.5	15.0	0.060
30	1.8	2.3	142.5	172.5	30.0	0.057
	2.4	4.3	52.5	37.5	15.0	0.099
	3.9	3.1	352.5	172.5	0.0	0.033
	2.7	2.9	352.5	360.0	7.5	0.076

MX-80, MilliQ water equilibrated

RH [%]	R_{max}	v_{max}	$\varphi_{maximum}$ (SAXD) [°]	$\varphi_{maximum}$ (XMT) [°]	Difference [°]	Porosity based on XMT
100	1.5	N/A	97.5	N/A	N/A	N/A
	1.4	N/A	262.5	N/A	N/A	N/A
	1.3	2.0	67.5	22.5	45.0	0.027
	1.2	2.3	127.5	172.5	45.0	0.013
85	1.2	3.3	67.5	15.0	N/A	0.002
	1.1	2.8	277.5	337.5	N/A	0.001
	1.1	1.8	187.5	157.5	30.0	0.006
	1.2	2.2	82.5	157.0	74.5	0.001
32	1.2	2.5	217.5	180.0	37.5	0.002
	1.1	1.9	112.5	15.0	82.5	0.003
	1.1	1.9	7.5	0.0	7.5	0.032
	1.3	1.7	82.5	172.5	90.0	0.053
	1.4	1.5	82.5	165.0	82.5	0.031

[a] High porosity due to part of the SAXD beam passing through the void between sample segments (visible e.g. in Fig. 3). This has some influence also on the orientation parameter values.

the diffraction analysis. Combining the microstructural information obtained with XMT and the detailed mineralogy could be useful in a wide variety of samples in the geophysical sciences, shales and clayrocks being the most prominent clay-bearing examples. Synchrotron X-ray microtomography and diffraction have successfully been applied by Kanitpanyacharoen et al. (2011, 2012) to study the mineral preferred orientation and associated micron-scale structure of shales; the methodology presented here could be used to shed new light on such materials through pinpointing the location of the diffracting beam within the

(potentially very heterogeneous) sample with ~200 μm precision. An added advantage of using an X-ray tube system is easier accessibility compared with limited beamtime on a synchrotron source.

5. Conclusions

We have combined X-ray microtomography with small-angle X-ray diffraction to show that uniaxial compaction of calcium montmorillonite results in strong preferred orientation of clay particles, which in turn
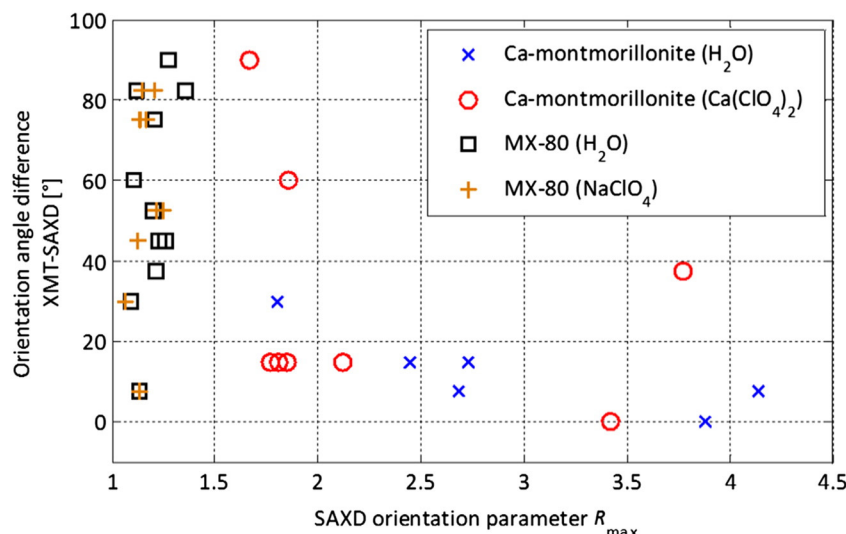

Fig. 7. Correlation of microcrack orientation observed with XMT and preferred orientation observed with SAXD, as a function of SAXD orientation parameter value.

results in a similarly oriented network of microcracks as the clay mineral shrinks during drying. MX-80 bentonite, on the other hand, exhibits nearly isotropic structure due to the essentially incompressible accessory minerals, which prevent the clay particles from forming a close-packed structure. Overall, the small-angle diffraction results presented agree well with previously published results. The novel experimental and data analysis method presented to quantify the orientation is readily applicable to other geological samples as well, provided the sample is suitably small to allow transmission of the scattering X-ray beam.

References

Andra, 2011. The deep geological disposal concept as developed by Andra. DCOM/11-0141. French National Radioactive Waste Management Agency, Châtenay-Malabry (Available online at http://www.andra.fr/international/download/andra-international-en/document/Andra_Geological.pdf. Retrieved 20.5.2014).

Bihannic, I., Tchoubar, D., Lyonnard, S., Besson, G., Thomas, F., 2001. X-ray scattering investigation of swelling clay fabric. J. Colloid Interface Sci. 240, 211–218.

Bradbury, M.H., Bayens, B., 2003. Porewater chemistry in compacted re-saturated MX-80 bentonite. J. Contam. Hydrol. 61, 329–338.

Cnudde, V., Boone, M.N., 2013. High-resolution X-ray computed tomography in geosciences: a review of the current technology and applications. Earth Sci. Rev. 123, 1–17.

Devineau, K., Bihannic, I., Michot, L., Villiéras, F., Masrouri, F., Cuisinier, O., Fragneto, G., Michau, N., 2006. In situ neutron diffraction analysis of the influence of geometric confinement on crystalline swelling of montmorillonite. Appl. Clay Sci. 31, 76–84.

Ferrage, E., Lanson, B., Sakharov, B.A., Drits, V.A., 2005. Investigation of smectite hydration properties by modeling experimental X-ray diffraction patterns. Part I. Montmorillonite hydration properties. Am. Mineral. 90 (8-9), 1358–1374.

Gimmi, T., Leupin, O.X., Eikenberg, J., Glaus, M.A., Van Loon, L.R., Waber, H.N., Wersin, P., Wang, H.A.O., Grolimund, D., Borca, C.N., Dewonck, S., Wittebroodt, C., 2014. Anisotropic diffusion at the field scale in a 4-year multi-tracer diffusion and retention experiment — I: insights from the experimental data. Geochim. Cosmochim. Acta 125, 373–393.

Greenspan, L., 1976. Humidity fixed points of binary saturated aqueous solutions. J. Res. Natl Bur. Stand. A 81A (1), 89–96.

Holmboe, M., Wold, S., Jonsson, M., 2012. Porosity investigation of compacted bentonite using XRD profile modelling. J. Contam. Hydrol. 128, 19–32.

Holzer, L., Münch, B., Rizzi, M., Wepf, R., Marschall, P., Graule, T., 2010. 3D-microstructure analysis of hydrated bentonite with cryo-stabilized pore water. Appl. Clay Sci. 47, 330–342.

Juvankoski, M., 2013. Buffer design 2012. Posiva Report 2012-14. Posiva Oy, Eurajoki Available online at http://www.posiva.fi/files/3355/POSIVA_2012-14.pdf. Retrieved 29.6.2014.

Kanitpanyacharoen, W., Wenk, H.-R., Kets, F., Lehr, C., Wirth, R., 2011. Texture and anisotropy in Qusaiba shales. Geophys. Prospect. 59, 536–556.

Kanitpanyacharoen, W., Kets, F., Wenk, H.-R., Wirth, R., 2012. Mineral preferred orientation and microstructure in the Posidonia shale in relation to different degrees of thermal maturity. Clay Clay Miner. 60 (3), 315–329.

Kawaragi, C., Yoneda, T., Tsutomu, S., Katsuhiko, K., 2009. Microstructure of saturated bentonites characterized by X-ray CT observations. Eng. Geol. 106, 51–57.

Keller, L.M., Holzer, L., Wepf, R., Gasser, P., 2011. 3D geometry and topology of pore pathways in Opalinus clay: implications for mass transport. Appl. Clay Sci. 52, 85–95.

Kohout, T., Kallonen, A., Suuronen, J.-P., Rochette, P., Hutzler, A., Gattacceca, J., Badjukov, D.D., Skála, R., Böhmová, V., Čuda, J., 2014. Density, porosity, mineralogy, and internal structure of cosmic dust and alteration of its properties during high velocity atmospheric entry. Meteorit. Planet. Sci. 49 (7), 1157–1170.

Matusewicz, M., Pirkkalainen, K., Liljeström, V., Suuronen, J.-P., Root, A., Muurinen, A., Serimaa, R., Olin, M., 2013. Microstructural investigation of calcium montmorillonite. Clay Miner. 48, 267–276.

Muurinen, A., Carlsson, T., 2013. Bentonite pore structure based on SAXS, chloride exclusion and NMR studies. Posiva Working Report 2013-53. Posiva Oy, Eurajoki (Available online at http://www.posiva.fi/files/3388/WR_2013-53.pdf. Retrieved 17.6.2014).

Nagra, 2002. Opalinus clay project, demonstration of feasibility of disposal ("Entsorgungsnachweis") for spent fuel, vitrified high-level waste and long-lived intermediate-level waste. Technical Report. Nagra: Swiss National Cooperative for the Disposal of Radioactive Waste, Wettingen (Available online at http://www.nagra.ch/data/documents/database/dokumente/$default/DefaultFolder/Publikationen/BroschuerenThemenhefte/e_bro_proj_opa.pdf. Retrieved 20.5.2014).

Norrish, K., 1954. The swelling of montmorillonite. Discuss. Faraday Soc. 18, 120–134.

Posiva, 2012. Safety case for the disposal of spent nuclear fuel at Olkiluoto — synthesis 2012, Posiva 2012-12. Technical Report. Posiva Oy, Eurajoki (Available online at http://www.posiva.fi/files/2987/Posiva_2012-12web.pdf. Retrieved 20.5.2014).

Saba, S., Barnichon, J.-D., Cui, Y.-J., Tang, A.M., Delage, P., 2014a. Microstructure and anisotropic swelling behaviour of compacted bentonite/sand mixture. J. Rock Mech. Geotech. Eng. 6, 126–132.

Saba, S., Delage, P., Lenoir, N., Cui, Y.J., Tang, A.M., Barnichon, J.-D., 2014b. Further insight into the microstructure of compacted bentonite–sand mixture. Eng. Geol. 168, 141–148.

Salles, F., Beurroies, I., Bildstein, O., Jullien, M., Raynal, J., Denovel, R., Van Damme, H., 2008. A calorimetric study of mesoscopic swelling and hydration sequence in solid Na-montmorillonite. Appl. Clay Sci. 39, 186–201.

Sato, H., Suzuki, S., 2003. Fundamental study on the effect of an orientation of clay particles on diffusion pathway in compacted bentonite. Appl. Clay Sci. 23, 51–60.

SKB, 2011. Long-term safety for the final repository for spent nuclear fuel at Forsmark, SKB TR-11-01. Technical Report. Svensk Kärnbränslehantering AB, Stockholm (Available online at http://skb.se/upload/publications/pdf/TR-11-01_vol1.pdf. Retrieved 24.6.2014).

Suuronen, J.-P., Kallonen, A., Hänninen, V., Blomberg, M., Hämäläinen, K., Serimaa, R., 2014. Bench-top X-ray microtomography complemented with spatially localized X-ray scattering experiments. J. Appl. Crystallogr. 47, 471–475.

Suzuki, S., Sato, H., Ishidera, T., Fujii, N., 2004. Study on anisotropy of effective diffusion coefficient and activation energy for deuterated water in compacted sodium bentonite. J. Contam. Hydrol. 68, 23–37.

Tributh, H., Lagaly, G., 1986. Aufbereitung und Identifizierung von Boden- und Lagerstättentonen. I. Aufbereitung der Proben im Labor. GIT Fachz. Lab. 30, 524–529.

Wenk, H.-R., Voltolini, M., Mazurek, M., Van Loon, L.R., Vinsot, A., 2008. Preferred orientations and anisotropy in shales: Callovo-Oxfordian shale (France) and Opalinus Clay (Switzerland). Clay Clay Miner. 56 (3), 285–306.